# Triboelectrification-Based Organic Film Nanogenerator for Acoustic Energy Harvesting and Self-Powered Active Acoustic Sensing

Jin Yang,[†,‡,⊥] Jun Chen,[†,⊥] Ying Liu,[†] Weiqing Yang,[†] Yuanjie Su,[†] and Zhong Lin Wang[*,†,§]

[†]School of Materials Science and Engineering, Georgia Institute of Technology, Atlanta. Georgia 30332-0245, United States, [‡]Department of Optoelectronic Engineering, Chongqing University, Chongqing 400044, China, and [§]Beijing Institute of Nanoenergy and Nanosystems, Chinese Academy of Sciences, Beijing 100083, China. [⊥]J.Y. and J.C. contributed equally to this work.

ABSTRACT As a vastly available energy source in our daily life, acoustic vibrations are usually taken as noise pollution with little use as a power source. In this work, we have developed a triboelectrification-based thin-film nanogenerator for harvesting acoustic energy from ambient environment. Structured using a polytetrafluoroethylene thin film and a holey aluminum film electrode under carefully designed straining conditions, the nanogenerator is capable of converting acoustic energy into electric energy *via* triboelectric transduction. With an acoustic sensitivity of 9.54 V Pa^{-1} in a pressure range from 70 to 110 dB and a directivity angle of 52°, the nanogenerator produced a maximum electric power density of 60.2 mW m^{-2}, which directly lit 17 commercial light-emitting diodes (LEDs). Furthermore, the nanogenerator can

also act as a self-powered active sensor for automatically detecting the location of an acoustic source with an error less than 7 cm. In addition, an array of devices with varying resonance frequencies was employed to widen the overall bandwidth from 10 to 1700 Hz, so that the nanogenerator was used as a superior self-powered microphone for sound recording. Our approach presents an adaptable, mobile, and cost-effective technology for harvesting acoustic energy from ambient environment, with applications in infrastructure monitoring, sensor networks, military surveillance, and environmental noise reduction.
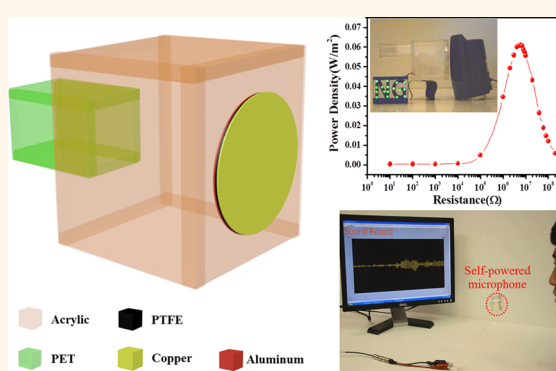
KEYWORDS: triboelectric nanogenerator · acoustic energy harvesting · self-powered acoustic sensing

As a clean, ubiquitous and sustainable energy source, acoustic waves, such as various sound noises from any living activities, airports, construction sites, and traffic, are one of the wasted energies that are abundant in our daily life. Sound energy is usually taken as unwanted noise that is polluting our living environment. Acoustic energy harvesting has not been as popular as other types of energy harvesting, such as solar energy and thermal electric energy, possibly because not only do sound waves have much lower power density but also there is a lack of effective technology for harvesting such energy.[1,2] Harvesting acoustic energy has been demonstrated using approaches based on piezoelectric[3−6] and electrostatic effects,[7]

but their performances are limited by low energy conversion efficiency,[3−5] low power density,[6] structure complexity,[5] and the requirement of high-quality materials.[7] Furthermore, most of the presented devices generally work at high frequencies from a few kilohertz to megahertz,[3,6,7] while sound sources available in everyday life contain predominantly low frequency components, making the presented mechanisms unsuitable in most circumstances.[8] Therefore, harvesting sound wave energy remains as a challenge.

Lately, we have developed innovative approaches for harnessing mechanical vibration energy using triboelectrification effect, which is an effect that has been known for thousands of years.[9−13] The creative

invention is proved to be capable of scavenging mechanical action/motion, such as random vibrations,[14] rotating motion,[15,16] wind and flowing water,[17] even ocean wave.[18] As a cost-effective, simple and robust approach, the triboelectric nanogenerators provide an effective means for ambient energy harvesting, and its performance is superior to any existing approaches of its kind.

Here, we report the first organic thin-film based triboelectric nanogenerator to scavenge ambient acoustic energy as a sustainable power source and self-powered active acoustic sensors in the low frequency range available in our daily life. By utilizing a Helmholtz cavity, the sensitivity of the as-fabricated device was as high as 9.54 V Pa^{-1} in the acoustic pressure range from 70 dB$_{SPL}$ (0.063 Pa) to 110 dB$_{SPL}$ (6.32 Pa), and the directional pattern is in a shape of Cardioid with a total response angle of 52°. With superior response to the sound waves, the rationally designed nanogenerator, operating at resonance frequency, produces a uniform signal output, with an open-circuit voltage up to 60.5 V, a short-circuit current amplitude of 15.1 μA, and a corresponding peak power density of 60.2 mW m^{-2} at 110 dB$_{SPL}$. The harvested acoustic energy is demonstrated to simultaneously light 17 commercial light emitting diodes (LEDs) connected in serials. Compared to the state-of-the-art acoustic energy harvesters, the superior output performance enables considerably high energy conversion efficiency up to ~60%. Furthermore, the as-prepared nanogenerator can also act as a self-powered active sensor for acoustic source detection and sound source positioning with an average error less than 7 cm, even if the distance between the source and the acoustic sensors (ASs) is more than hundreds of meters. In addition, the working bandwidth of the proposed nanogenerator can be effectively widened when an array of devices with varying resonance frequencies operating together. With an overall bandwidth from 10 to 1700 Hz, the fabricated organic film nanogenerators are capable of serving as a self-powered microphone for sound recording. The concept and design presented in this work can be further applied in a variety of other circumstances for either energy-harvesting or sensing purposes, e.g., aeroacoustic sensing, jet engine noise reduction, implantable human ear, and wireless technology applications.

RESULTS AND DISCUSSION

Relying on a Helmholtz cavity with a size-tunable narrow neck on its back, the core of the nanogenerator is in a circular shape and embedded as the flexible front plate of the cavity, as schematically shown in Figure 1a. For a better illustration, a cross-sectional view of the core is shown in Figure 1b, with a multi-layered structure. Aluminum thin film with nanoporous surface plays dual roles as an electrode and a contact
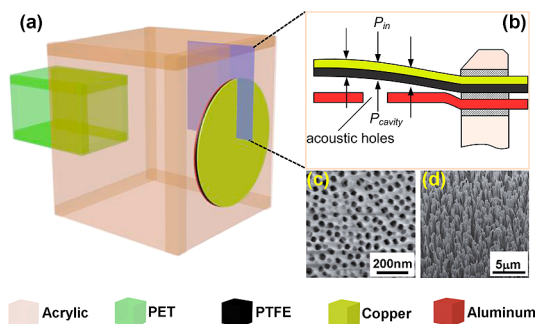

Figure 1. Structural design of the organic film nanogenerators. (a) Sketch and (b) cross-sectional view of the nanogenerator. (c) SEM image of nanopores on aluminum electrode. (d) SEM image of PTFE nanowires fabricated on the film surface by plasma etching, which largely increase the triboelectrification.

surface. A scanning electron microscopy (SEM) image of nanopores on the aluminum is presented in Figure 1c. The nanopores were uniformly distributed on the surface of aluminum with an average diameter of 57 ± 5 nm and a density of 210 per μm^2. A layer of polytetrafluoroethylene (PTFE) film with deposited copper was employed as another electrode. An SEM image of the PTFE nanowires is displayed in Figure 1d. The average diameter of PTFE nanowires is 54 ± 3 nm with an average length of 1.1 ± 0.4 μm. The fabrication process in detail is discussed in the Methods.

When an external sound wave is incident on the core part of the nanogenerator, the air within the cavity is alternately compressed and expanded in response to the magnitude and frequency of the sound wave, and thus, the PTFE thin film will oscillate due to the initiated pressure difference on its two sides while the aluminum film stays still. Mathematically, the pressure difference can be expressed as[19]

$$\Delta p = 2p \sin(kd \cos\theta/2) \qquad (1)$$

where k is the wavenumber, p is the incident acoustic pressure, d is the effective distance between the PTFE thin film and the opening of the neck, and θ is the sound wave incident angle, which is the angle between the sound propagation direction and the normal direction of the PTFE surface.

A MATLAB simulation for the deformation of the PTFE film under the acoustic pressure difference is shown in Figure 2a, where we assume that the uniformly distributed acoustic pressure difference is 0.1 Pa and the Young's modulus of the cylindrical PTFE thin film (65 mm in diameter and 0.06 mm in thickness) is 420 MPa. The color represents the magnitude of the deformations of the PTFE thin film, of which a maximum displacement of 0.7 mm is obtained at the center. The average deformation is a monotonically increasing function of acoustic pressure difference throughout our experimental time window, as shown in Figure 2b.
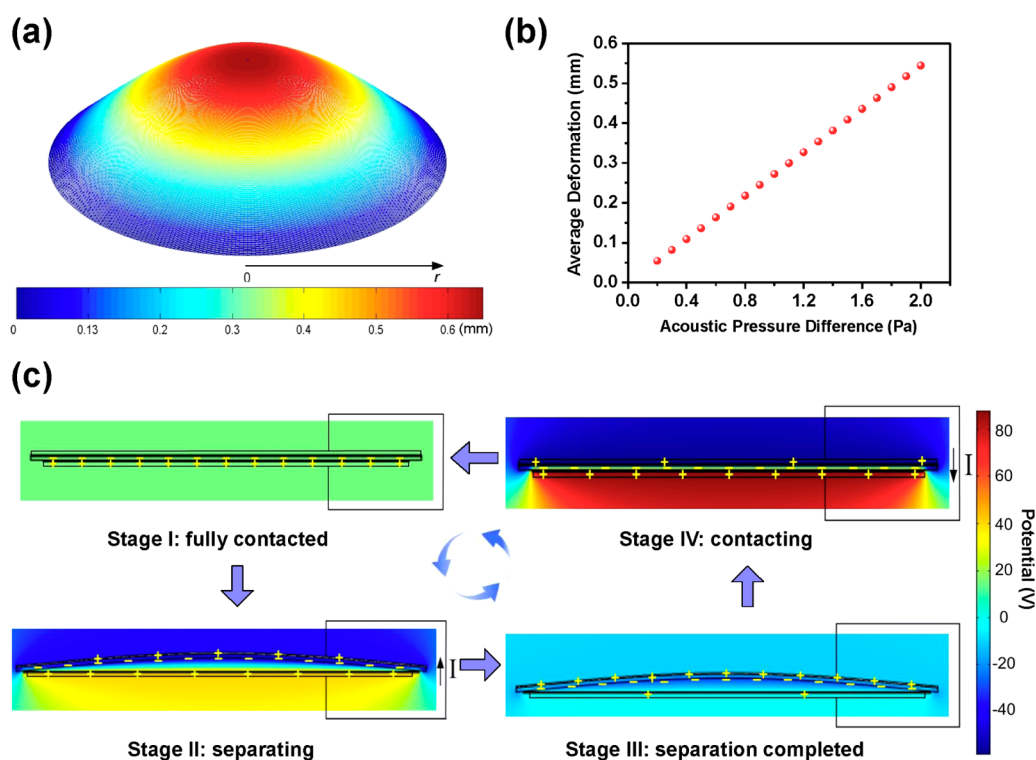
(a)

(b)

(c)

Figure 2. Working principle of the organic film nanogenerators. (a) Simulation result of PTFE thin film oscillating mode. (b) Relationship between the average deformation of the PTFE thin film and the acoustic pressure difference. (c) COMSOL simulation of the periodic potential change between the two electrodes upon acoustically induced cyclic deformation, showing the driving force for the back-and-forth charge flow generated by the nanogenerator.

A cycle of electricity generation process under acoustic pressure is schematically depicted in Figure 2c using the numerically simulated electrostatic potential distribution arising from triboelectric charges (using COMSOL package). In its original state, the PTFE is in contact with aluminum thin film. Because PTFE is much more triboelectrically negative than aluminum, electrons are injected from aluminum into PTFE, generating positive triboelectric charges on the aluminum side and negative charges on the PTFE side (Figure 2c, stage I). Due to the wave character of sound propagation, a resulting acoustic pressure separates the PTFE thin film away from the aluminum thin film. As a result, the positive triboelectric charges and the negative ones no longer coincide on the same plane and an inner dipole moment between the two contact surfaces is consequently generated, which drives free electrons to flow from the copper electrode to the aluminum electrode to screen the local electric field, producing positively induced charges on the copper electrode (Figure 2c, stage II). The flow of electrons lasts until the PTFE thin film reaches the highest point, where the corresponding separation is maximized (Figure 2c, stage III). Subsequently, due to the acoustic pressure difference change, the PTFE film is pushed back toward the aluminum film. In response to the reduced separation and thus the weakened potential drop, the free electrons in aluminum electrode flow back to the copper electrode until the two surfaces come into contact, making a complete cycle of electricity generation (Figure 2c, stage IV). Then the PTFE thin film is bounced away from the aluminum thin film again after obtaining a momentum from the sound waves, starting another cycle of electricity generation. The output electric signal can be a power source or a sound sensor, as illustrated in the following discussion.

To investigate the performance of the proposed nanogenerator in harvesting acoustic energy, a loudspeaker (Fostex, Inc.) that provides sinusoidal sound waves was used as an acoustic source with tunable frequency and amplitude. A sound level meter (Extech, Inc.) with 2 dB accuracy and 0.1 dB resolution is used to measure the incident acoustic pressure. The meter is located near the harvester at a distance far less than the acoustic wavelength.

Displacements in the radial direction are prescribed at the outer circular boundary of the PTFE film to intentionally introduce the initial in-plane prestress in order to tune the resonance frequency of the film, thus rendering it an elastic element to oscillate under acoustic wave excitation. Under prestresses of 2.8, 5.6, and 8.4 kPa and a constant incident acoustic pressure of 110 dB_{SPL}, the reliance of open-circuit voltages (V_{oc}) and short-circuit currents (I_{sc}) on the input acoustic frequency is presented in parts a and b, respectively, of Figure 3. At the resonance frequencies, the V_{oc} under different prestresses are respectively 16.50, 60.50, and 7.50 V, respectively, while I_{sc} are 5.50, 15.10, and 2.10 μA,
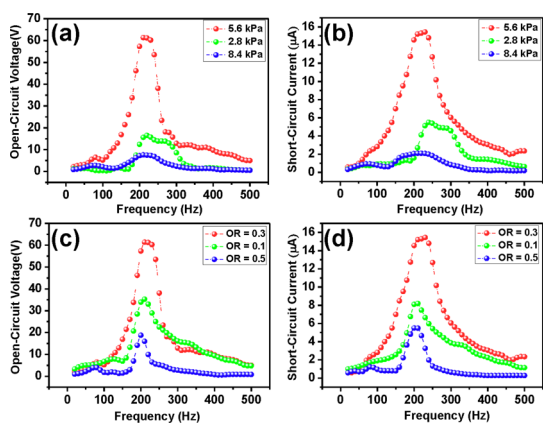
Figure 3. Electrical measurement of the organic film nanogenerators. (a) Open-circuit voltages (V_{OC}) and (b) short-circuit currents (I_{SC}) as a function of acoustic frequency with different prestresses of 2.8, 5.6, and 8.4 kPa. The curves are the fitted results. (c) V_{OC} and (d) I_{SC} as a function of acoustic frequency with different open ratios (ORs) of 0.1, 0.3, and 0.5. The curves are the fitted results.

respectively. The output voltage shows an enhancement of 3.7 times for the device with a prestress of 5.6 kPa than that with the prestress of 2.8 kPa, and also an enhancement of 8.1 times is achieved compared to the device with prestress of 8.4 kPa. The results show that a suitable initial prestress can optimize the oscillation coupling between the air trapped in the cavity and PTFE thin film and, thus, the electrical output.

Regarding the optimized design, namely, the device with prestress of 5.6 kPa, experimentally, both V_{oc} and I_{sc} are maximized at the acoustic frequency of 240 Hz, indicating that 240 Hz is the resonance frequency of the as-fabricated generator. The output voltage and current at the resonance frequency of 240 Hz are demonstrated in Figure S1 (Supporting Information). Theoretically, if the dimensions of the device are smaller than or comparable to the incident acoustic wavelength, its dynamic behavior can be modeled as a lumped system and its resonant frequency can be expressed as[20]

$$f_R = \frac{c}{2\pi}\sqrt{\frac{S}{L'V}} \qquad (2)$$

where S and L' are, respectively, the cross-sectional area and effective length of the neck, V is the cavity volume, and c is the speed of sound in air (343 m s^{-1}). Submitting the values into eq 2, we can obtain the theoretical natural frequency of 238.8 Hz, which is consistent with the experimental results.

In addition, the prestress has a marked impact on the electric output of the device, aimed at further improving the electric output, and a series of acoustic holes are punched through the aluminum electrode, which act as communicating vessels to integrate the air gap between two contact surfaces with the air in the cavity. The open ratio (OR) is defined as the area ratio of all acoustic holes' area to the surface area of the

aluminum electrode, which largely influences the damping of the air. A larger value of OR results in a higher flow velocity and lower damping,[21] which will contribute to a larger deformation of the PTFE film under the same acoustic pressure excitation. Under a constant acoustic pressure of 110 dB$_{SPL}$, the V_{oc} and I_{sc} of the generator with different ORs of 0.1, 0.3, and 0.5 were respectively measured, as shown in parts c and d of Figure 3. At the resonance frequencies, the V_{oc} for open ratios of 0.1, 0.3, and 0.5 are, respectively, 35.20, 60.50, and 18.70 V, and the corresponding I_{sc} are 8.20, 15.10, and 5.50 μA. The results indicate that an enhancement of 1.7 times the electric output is obtained for the device with an OR value of 0.3, compared to that of 0.1, and also an enhancement of 3.2 times is achieved compared to that of 0.5. This experimental observation is resulted from a trade-off between the PTFE deformation and the effective contact area. Larger OR leads to a larger deformation of the PTFE thin film and thus a higher electric output. However, increased OR will reduce the effective contact area for triboelectrification, and thus a lower electrical output. Consequently, an optimum OR is needed to maximize the electrical output.

Upon the optimization of device design with appropriate prestress and OR, a further step is made toward investigating the relationship between the device electrical outputs and applied acoustic power and frequency. The acoustic frequencies are spreading from 0 to 500 Hz, and the corresponding acoustic pressure ranging from 70 dB$_{SPL}$ to 110 dB$_{SPL}$ in a step of 5 dB$_{SPL}$ is controlled and measured by the sound level meter. The electric output is highly related to the input acoustic pressures and frequencies, and detailed relationships are demonstrated in Figure 4a,b. As shown, at the resonant frequency of 240 Hz, with decreasing acoustic pressure from 110 dB$_{SPL}$ to 70 dB$_{SPL}$, the V_{oc} is decreased from 60.50 to 0.73 V and the short-circuit current is decreased from 15.10 to 0.19 μA. Based on the experimental results, a MATLAB fitting renders a linear relationship between the open-circuit voltage (V_{oc}) and the applied acoustic pressure P_{in} (in Pascal), which can be expressed as

$$V_{oc} = 9.54P_{in} + 0.13 \qquad (3)$$

The sensitivity of the generator as a pressure sensor was 9.54 V Pa^{-1} in the acoustic pressure range from 0.063 Pa (70 dB$_{SPL}$) to 6.32 Pa (110 dB$_{SPL}$) at a frequency of 240 Hz.

Furthermore, the acoustic waves decay in the course of propagation; thus, the distance of the measured device to the acoustic source shows a tremendous impact on the electric output for acoustic energy harvesters. At a fixed acoustic pressure of 110 dB$_{SPL}$ and resonant frequency of 240 Hz, a distance depended electric output is measured, as shown in Figure 4c. The open-circuit voltage is decreased from
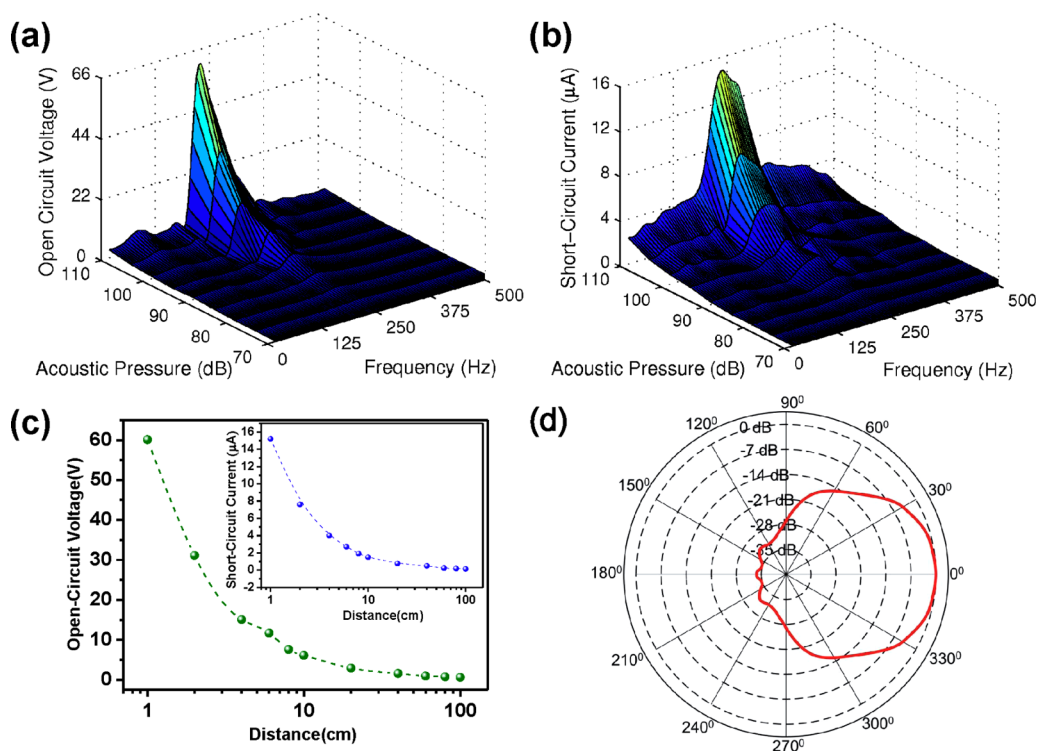
(a)

(b)

(c)

(d)

Figure 4. Electrical and acoustical performance evaluation of the organic film nanogenerators. (a) V_{OC} and (b) I_{SC} as a function of acoustic pressures and frequencies. (c) Nanogenerator acts as an active acoustic sensor for distance measurement as well as ambient acoustic source detection. When a sound source approaching the nanogenerator, the output signal is exponentially increased. (d) Directional pattern of the nanogenerator.

60.50 to 0.81 V, with short-circuit current decreasing from 15.10 to 0.21 μA when the distance is increased from 1 to 100 cm. It is worth noting that the electric output attenuates at a rate of 6 dB each time the distance from the acoustic source doubles.

For a comprehensive study of the proposed acoustic energy harvester, we took a further step to evaluate the directional dependence (directivity) pattern of the as-fabricated devices. We anchored the device onto a rotary stage and then gradually increased the rotating angle from 0 to 360° and measured the V_{oc} at the resonant acoustic frequency of 240 Hz. The corresponding directional pattern is obtained by normalizing relative to the peak response of voltage, as illustrated in Figure 4d. The test results show that the pattern is in shape of Cardioid and smooth as a function of rotating angle, and the −3 dB points are at +26° and −26° off axis, producing a total response angle of 52°. At an angle of 90°, the sound pressure level is reduced to −28 dB from the maximum value on-axis. The acoustic response of the device has a dependence on the incident angle of the sound waves, which is actually the stage rotating angle in the measurement. As a sound filter, the as-fabricated device is sensitive to the sound coming from directions within the response angle and rejects the contribution from other angles, which renders it a great potential in the application of directional microphones.

Resistors were utilized as external loads to further investigate the useful output power of the as-fabricated nanogenerator at the resonance frequency. As displayed in Figure 5a, the voltage amplitudes increase with increasing load resistance, while the current follows a reverse trend owing to the Ohmic loss. As a result, the instantaneous peak power $(V^2/R)_{peak}$ is maximized at a load resistance of 6 MΩ, corresponding to a peak power density of 60.2 mWm^{-2} (Figure 5b). To prove the capability of the proposed nanogenerator as a sustainable power source, powered by a nanogenerator with the cavity dimensions of 8 cm × 8 cm × 8 cm under acoustic pressure of 110 dB$_{SPL}$ at the resonant frequency of 240 Hz, 17 commercial LED bulbs were lit simultaneously, as demonstrated in the inset of Figure 5b, as visualized in supporting movie 1 (Supporting Information).

As an acoustic energy harvester with superior output performance, the as-fabricated nanogenerators are also capable of acting as active self-powered acoustic sensors. A series of practical applications were demonstrated. The first demonstration for the nanogenerators is to act as a self-powered microphone. The natural frequencies of the devices can be designed by parameters configuration, and their corresponding frequency bands are able to overlap with each other, rendering us a broadened working bandwidth. Here, as demonstrated in Figure 6a, four nanogenerators, NG$_1$, NG$_2$, NG$_3$, and NG$_4$, respectively, with dimensions
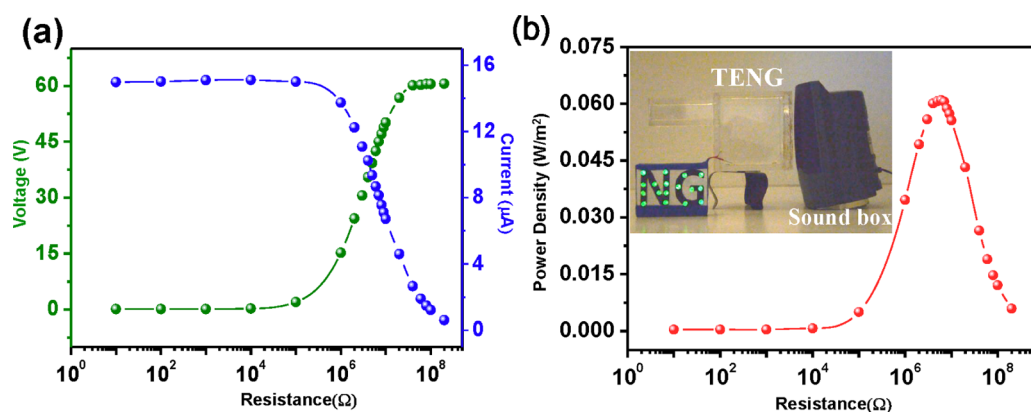
Figure 5. Demonstration of the organic film nanogenerator acting as a sustainable power source. (a) Dependence of the voltage and current output on the external load resistance. The points represent peak value of electric signals, while the lines are the fitted results. (b) Dependence of the peak power output on the resistance of the external load, indicating maximum power output at $R = 6$ MΩ. The curve is the fitted result. Inset is a photograph that shows how the nanogenerator works under excitation from a sound box. Due to the external sound, 17 LEDs are being lighted up simultaneously.
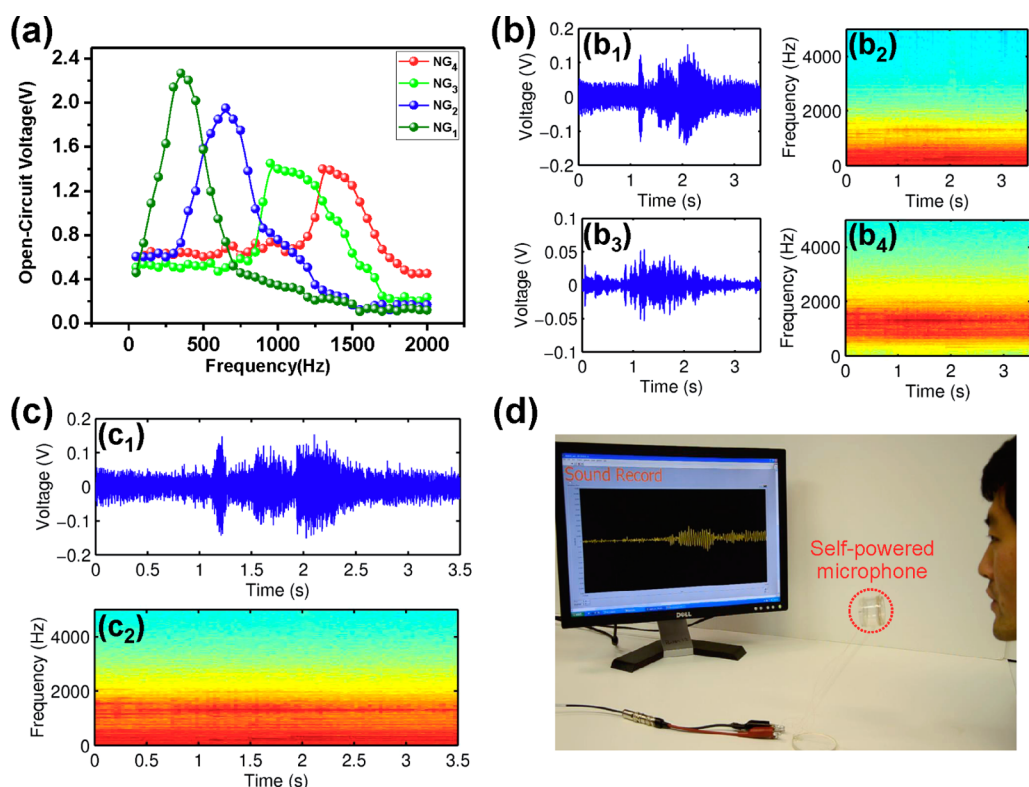

Figure 6. Demonstration of the organic film nanogenerator acting as a self-powered microphone. (a) Frequency responses from the nanogenerators array, which consists of four NGs with various designed natural frequencies, aimed to enhance the overall working bandwidth. (b_1, b_2) Sound waveforms of the signals acquired by NG_1 and NG_2, respectively. (b_3, b_4) Short-time Fourier transforms of the acquired signals by NG_1 and NG_2, respectively. (c) Sound waveform and corresponding short-time Fourier transform of the signals acquired by the array of the NGs. (d) Photograph that shows a NG is working as a self-powered microphone for sound recording.

of 11 mm × 11 mm × 11 mm, 9 mm × 9 mm × 9 mm, 7 mm × 7 mm × 7 mm, and 5 mm × 5 mm × 5 mm, corresponding to resonance frequencies of 350, 650, 1100, and 1400 Hz, were employed to widen the overall working bandwidth from 10 to 1700 Hz, which assured the superior performance of the nanogenerators as a self-powered microphone for sound recording. For experimental measurements, a multichannel signal

acquisition implant was designed by LabVIEW to collect the electric outputs at a sampling rate of 44.1 kHz. Parts b_1 and b_3 of Figure 5 are, respectively, the time domain waveforms of the recorded sounds from NG_1 and NG_4. Although NG_1 and NG_4 share the same sound source, the waveforms of the two apparently exhibit different characteristics, which is attributed to a different frequency response ranges of the two. With a
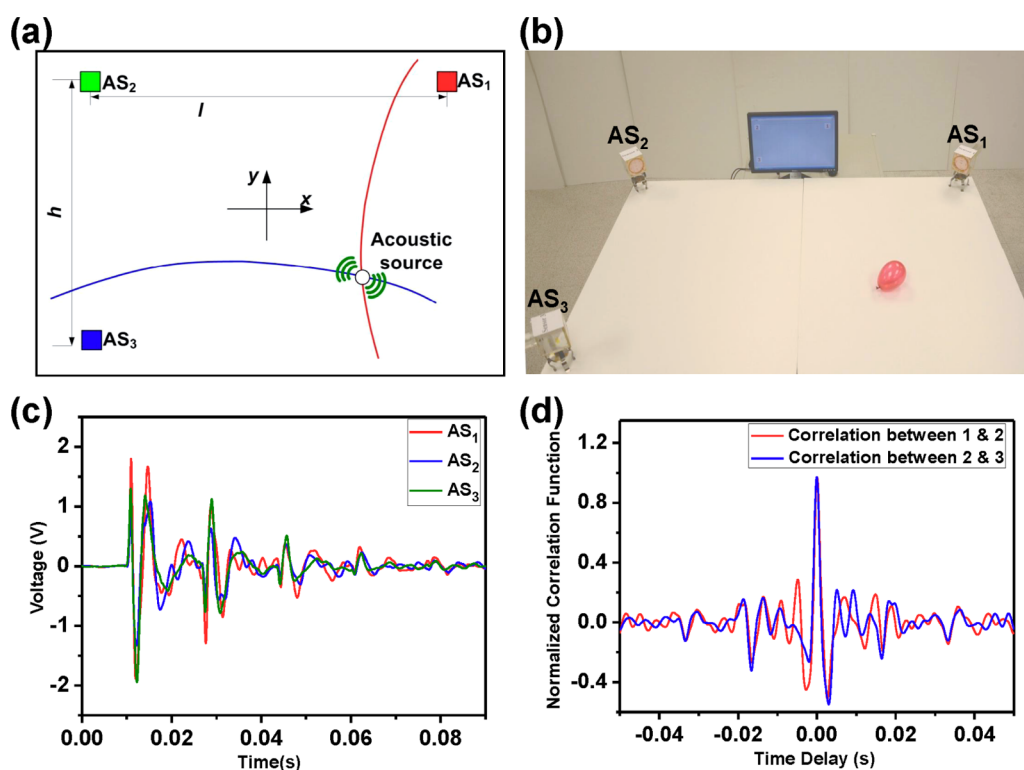
Figure 7. Demonstration of the organic film nanogenerator acting as an active sensor for acoustic source localization. (a) Schematic illustrations and (b) photograph showing the working mechanism of nanogenerators for sound localization. (c) Acquired acoustic signals from the three nanogenerators when a balloon burst. (d) Correlation functions of the acquired acoustic signals from AS 1, 2 and 3.

natural frequency of 350 Hz, the waveform of NG_1 is smoother owing to its dominant response to lower frequency components from 10 to 600 Hz, as shown in Figure 5b$_2$, which is the corresponding short-time Fourier transform (STFT), while the waveform of NG_4 with a natural frequency of 1400 Hz is rougher, due to its dominant response to the higher frequency components from 1100 to 1700 Hz, as demonstrated in Figure 5b$_4$ of its corresponding STFT.

In order to reconstruct the original sound, the acquired acoustic signals of the array are weighted according to the relative amount of information available from each source. The reconstructed signal S_{re} can be mathematically expressed as

$$S_{re} = \sum_{i=1}^{4} a_i s_i \qquad (4)$$

where a_i is a weighting factor, which is a function of speech-to-noise following a rule of $\sum_{i=1}^{4} a_i = 1$ and s_i is the acquired output acoustic signal from NG_i ($i = 1-4$).

The waveform of the reconstructed signal by eq 4 and its corresponding STFT are illustrated in parts c$_1$ and c$_2$, respectively, of Figure 6. The frequency components of the reconstructed signal cover all the frequencies ranging from 10 to 1700 Hz, as demonstrated in Figure 6c$_2$. Figure 6d shows an as-fabrication nanogernator working as a self-powered microphone

for sound recording, as visualized in supporting movie 2 (Supporting Information).

The second demonstration of the nanogenerator for sensing purpose is to act an acoustic source localization sensor. Experimentally, three as-fabricated nanogenerators were arranged in an L shape and anchored in a 2-dimensional (2D) plane with dimensions of 2 m by 1.8 m, as schematically shown in Figure 7a and a corresponding photograph in Figure 7b. The sound was created by bursting a small balloon in the 2D plane as acoustic sources. A customized triple-channel data acquisition system based on LabVIEW was used to collect the sensing signals from ASs. Figure 7c elucidates the acoustic signals acquired by the ASs when a balloon burst at the center of the 2D plane. When another balloon bursting spot is settled with various distances to the ASs, the three acoustic signals show obvious discrepancies in response starting time and magnitude, as demonstrated in Figure S2a (Supporting Information).

The acoustic localization algorithm presented in this work is based on the estimation of the time difference of arrival (TDOA) at pairs of acoustic sensors. Let $S_k = [X_k, Y_k]^T$ denote the location of kth AS with $k = 1$, 2, 3. Let $P = [x, y]^T$ represents the location of the acoustic source. Then, the distance $d(P, S_k)$ between acoustic source and the kth sensor can be expressed as

$$d(P, S_k) = ||S_k - P|| \qquad (5)$$

and the time delay in TDOA at S_i and S_j is given by

$$\tau_{ij}(P) = (d(P, S_i) - d(P, S_j))/c \qquad (6)$$

where $i, j = 1-3$ and $i \neq j$. The in-pair evaluating TDOA of acquired signals by ASs can be achieved by computing the cross-correlation function of these two signals. Let $z_i(n)$ and $z_j(n)$ denote the signals acquired by AS_i and AS_j, respectively, where n is the sample time index. Then, the cross-correlation function $R_{zi,zj}(\tau)$ between AS_i and AS_j is defined as

$$R_{z_i, z_j}(\tau) = \sum_{n=1}^{N} z_i(n)z_j(n + \tau_{ij}) \qquad (7)$$

where N is the number of the sample points. The time difference between the two acquired signals is estimated by the time lag at the highest peaks of their cross-correlation functions. Two correlation functions of the three acquired acoustic signals in Figure 7c were derived from eq 7, as shown in Figure 7d. It is worth noting that the time lags of the two cross-correlation functions between AS_1 and AS_2 as well as AS_2 and AS_3 are zero, indicating the same distance is traveled by the sound from the acoustic source to the ASs, which is well consistent with the real experimental case. For the case of acoustic source with various distances to the ASs, two cross-correlation functions calculated based on Figure S2a (Supporting Information) are demonstrated in Figure S2b (Supporting Information), from which the values of τ_{12} and τ_{23} are obtained, and equal to -1.3 and 3 ms, respectively, consistent with the experimental results. Give the distances between the three acoustic sensors and also the in-pair time delay information, the acoustic source can be localized/positioned as the intersection of the two hyperbolic curves by virtue of the speed of sound and geometry.[22] Experimentally, positioning within an average error circle of 7 cm in diameter is achieved based on multiple measurements, which mainly depends on the signal-to-noise ratio (SNR)[23] if the SNR of the acquired signals are comparable with each other, and the error will stay within a same average error circle even if the distance between the source and the ASs is more than hundreds of meters. A visualized demonstration of the nanogenerators for acoustic source localization is presented in supporting movie 3 (Supporting Information). The proposed acoustic sensors in this work have extensive applications in fields such as military surveillance and reconnaissance, intruder detection, sniper localization, underwater acoustics, and auto talker detection in a web conferencing.

Additionally, the as-fabricated nanogenerator can be harnessed for mass measurement. The working principle of mass measurement is schematically demonstrated (Figure S3a, Supporting Information). Different loads will lead to different deformations of the membrane under the same sound pressure excitation and, thus, different output voltages of the acoustic sensors. Experimental results show that the voltage output is a monotonically decreasing function of the applied mass throughout our experimental time window with a sensitivity of 270 mV/mg (Figure S3b, supporting movie 4, Supporting Information). By virtue of the triboelectric effect based mass measurement, the weight increment of the applied mass can also be measured.

CONCLUSIONS

We developed a new type of acoustic energy harvester that scavenges energy using triboelectrification effect, a universal phenomenon upon contact between two materials with opposite triboelectric polarities. Rationally designed structure, coupled with nanomaterial modification, the as-fabricated nanogenerator enables superior performance in harvesting ambient acoustic energy. It produced a maximum electric power density of 60.2 mW·m^{-2}, which directly lighted up 17 commercial LEDs simultaneously. The as-fabricated nanogenerators were also proved to be active self-powered acoustic sensors for sound recording, acoustic source localization, as well as mass measurement. This work not only presents an adaptable, cost-effective, and fundamentally new approach for ambient acoustic energy harvesting but also a milestone progress in nanogenerator-based active sensors. The concept and design presented in this work can be further applied in a variety of circumstances for either energy-harvesting or sensing purposes, e.g., aeroacoustic sensing, jet engine noise reduction, military surveillance, and reconnaissance as well as wireless technology applications.

METHODS

Nanopore-Based Aluminum Surface Modification. The electrochemical anodization was applied on aluminum foil in 3% (mass fraction) oxalic acid (H$_2$C$_2$O$_4$) electrolyte. The aluminum foil was anodized under a bias voltage of 30 V for 5 h with a platinum plate acting as the cathode. After that, the alumina layer was etched away in a solution of chromic acid (20 g L^{-1}) at 60 °C for 2 h. Then the aluminum foil was rinsed with DI water and dried in air.

Nanowire-Based PTFE Surface Modification. A PTFE film (50 μm thick) was first washed using menthol, isopropyl alcohol, and deionized water. Then, a layer of 100 nm copper was deposited onto this PTFE thin film using DC sputter for the etching process. Subsequently, the inductively coupled plasma (ICP) reactive ion etching was used to fabricate the aligned nanowires on the PTFE surface. O$_2$, Ar, and CF$_4$ gases were injected into the ICP chamber with a flow ratio of 10.0, 15.0, and 30.0 sccm, respectively. A large density of plasma was produced by a power source of 400 W, and another power source of 100 W was used to accelerate the plasma ions. The PTFE nanowires with an average length of ~1.1 μm were obtained after the PTFE film was etched for 40 s.

Fabrication of the Nanogenerator. To fabricate the nanogenerator, a cubic cavity with dimensions of 80 mm by 80 mm by 80 mm was first constructed using acrylic sheet (thickness of 0.25 in.). A narrow neck with dimensions of 28 mm × 28 mm × 80 mm is anchored into the back plate of the cavity. The core of the nanogenerator is in a circular shape with a diameter of 65 mm and embedded as the flexible front plate of the cavity. The core part has a multilayer structure. Aluminum thin film with a thickness of 0.5 mm plays dual roles of an electrode and a contact surface. Eight acoustic holes with diameter of 12.6 mm are designed into the aluminum electrode acting as communicating vessels to integrate the air gap between two contact surfaces with the air in the cavity. A layer of copper was deposited onto the PTFE film with thickness of 50 μm as another electrode.

Conflict of Interest: The authors declare no competing financial interest.

Supporting Information Available: Electrical measurement of the organic film nanogenerator; demonstration of the organic film nanogenerator acting as an active sensor for acoustic source localization; demonstration of the organic film nanogenerator acting as a self-powered acoustic sensor for mass measurement; supporting movies 1−4. This material is available free of charge *via* the Internet at http://pubs.acs.org.

REFERENCES AND NOTES

1. Wang, X. D.; Song, J. H.; Wang, Z. L. Direct-Current Nanogenerator Driven by Ultrasonic Waves. *Science* **2007**, *316*, 102–105.
2. Wang, X. D.; Liu, J.; Song, J. H.; Wang, Z. L. Integrated Nanogenerators in Biofluid. *Nano Lett.* **2007**, *7*, 2475–2479.
3. Cha, S. N.; Seo, J-. S.; Kim, S. M.; Kim, H.; Park, Y. J.; Kim, S.; Kim, J. M. Sound-Driven Piezoelectric Nanowire-Based Nanogenerators. *Adv. Mater.* **2010**, *22*, 4726–4730.
4. Xu, C.; Wang, X. D.; Wang, Z. L. Nanowire Structured Hybrid Cell for Concurrently Scavenging Solar and Mechanical Energies. *J. Am. Chem. Soc.* **2009**, *131*, 5866–5872.
5. Hansen, B. J.; Liu, Y.; Yang, R.; Wang, Z. L. Hybrid Nanogenerator for Concurrently Harvesting Biomechanical and Biochemical Energy. *ACS Nano* **2010**, *4*, 3647–3652.
6. Yang, R.; Qin, Y.; Dai, L.; Wang, Z. L. Power Generation with Laterally-Packaged Piezoelectric Fine Wires. *Nat. Nanotechnol.* **2009**, *4*, 34–39.
7. Que, R. H.; Shao, Q.; Li, Q. L.; Shao, M. W.; Cai, S. D.; Wang, S. D.; Lee, S. T. Flexible Nanogenerators Based on Graphene Oxide Films for Acoustic Energy Harvesting. *Angew. Chem., Int. Ed.* **2012**, *51*, 5418–5422.
8. Mei, J.; Ma, G. C.; Yang, M.; Yang, Z. Y.; Wen, W. J.; Sheng, P. Dark Acoustic Metamaterials as Super Absorbers for Low-Frequency Sound. *Nat. Commun.* **2012**, *3*, 756.
9. Fan, F. R.; Tian, Z. Q.; Wang, Z. L. Flexible Triboelectric Generator!. *Nano Energy* **2012**, *1*, 328–334.
10. Zhu, G.; Pan, C. F.; Guo, W. X.; Chen, C. Y.; Zhou, Y. S.; Yu, R. M.; Wang, Z. L. Triboelectric-Generator-Driven Pulse Electrodeposition for Micropatterning. *Nano Lett.* **2012**, *12*, 4960–4965.
11. Zhu, G.; Chen, J.; Liu, Y.; Bai, P.; Zhou, Y. S.; Jing, Q. S.; Pan, C. F.; Wang, Z. L. Linear-Grating Triboelectric Generator Based on Sliding Electrification. *Nano Lett.* **2013**, *13*, 2282–2289.
12. Yang, J.; Chen, J.; Yang, Y.; Zhang, H. L.; Yang, W. Q.; Bai, P.; Su, Y. J.; Wang, Z. L. Broadband Vibrational Energy Harvesting Based on a Triboelectric Nanogenerator. *Adv. Energy Mater.* **2013**, 10.1002/aenm.201301322.
13. Yang, W. Q.; Chen, J.; Zhu, G.; Yang, J.; Bai, P.; Su, Y. J.; Jing, Q. S.; Cao, X.; Wang, Z. L. Harvesting Energy from the Natural Vibration of Human Walking. *ACS Nano* **2013**, *7*, 11317–11324.
14. Chen, J.; Zhu, G.; Yang, W. Q.; Jing, Q. S.; Bai, P.; Yang, Y.; Hou, T. C.; Wang, Z. L. Harmonic-Resonator-Based Triboelectric Nanogenerator as a Sustainable Power Source and a Self-Powered Active Vibration Sensor. *Adv. Mater.* **2013**, *25*, 6094–6099.
15. Bai, P.; Zhu, G.; Liu, Y.; Chen, J.; Jing, Q. S.; Yang, W. Q.; Ma, J.; Zhang, G.; Wang, Z. L. Cylindrical Rotating Triboelectric Nanogenerator. *ACS Nano* **2013**, *7*, 6361–6366.
16. Lin, L.; Wang, S. H.; Xie, Y. N.; Jing, Q. S.; Niu, S. M.; Hu, Y. F.; Wang, Z. L. Segmentally Structured Disk Triboelectric Nanogenerator for Harvesting Rotational Mechanical Energy. *Nano Lett.* **2013**, *13*, 2916–2923.
17. Yang, Y.; Zhu, G.; Zhang, H. L.; Chen, J.; Zhong, X. D.; Lin, Z. H.; Su, Y. J.; Bai, P.; Wen, X. N.; Wang, Z. L. Triboelectric Nanogenerator for Harvesting Wind Energy and as Self-Powered Wind Vector Sensor System. *ACS Nano* **2013**, *7*, 9461–9469.
18. Hu, Y. F.; Yang, J.; Jing, Q. S.; Niu, S. M.; Wu, W. Z.; Wang, Z. L. Triboelectric Nanogenerator Built on Suspended 3D Spiral Structure as Vibration and Positioning Sensor and Wave Energy Harvester. *ACS Nano* **2013**, *7*, 10424–10432.
19. Sessler, G. M.; West, J. E. First-Order Gradient Microphone Based on the Foil-Electret Principle: Discrimination Against Air-Borne and Solid-Borne Noises. *J. Acoust. Soc. Am.* **1969**, *46*, 1081–1086.
20. Hu, X. H.; Ho, K. M. Homogenization of Acoustic Metamaterials of Helmholtz Resonators in Fluid. *Phys. Rev. B.* **2008**, *77*, 172301.
21. Her, H. C.; Wu, T. L.; Huang, J. H. Acoustic Analysis and Fabrication of Microelectromechanical System Capacitive Microphones. *J. Appl. Phys.* **2008**, *104*, 084509.
22. Kundu, T. Acoustic Source Localization. *Ultrasonics* **2014**, *54*, 25–38.
23. Jacovitti, G.; Scarano, G. Discrete Time Techniques for Time Delay Estimation. *IEEE Trans. Signal Process.* **1993**, *41*, 525–533.